Eur. Phys. J. A **24**, 343–353 (2005)
DOI 10.1140/epja/i2005-10034-2

THE EUROPEAN PHYSICAL JOURNAL A

Equivalence between local Fermi gas and shell models in inclusive muon capture from nuclei

J.E. Amaro[1,a], C. Maieron[2], J. Nieves[1], and M. Valverde[1]

[1] Departamento de Física Moderna, Universidad de Granada, Granada 18071, Spain
[2] INFN, Sezione di Catania, Via Santa Sofia 64, 95123 Catania, Italy

Received: 14 February 2005 / Revised version: 10 April 2005 /
Published online: 2 June 2005 –
Communicated by A. Molinari

Abstract. Motivated by recent studies of inclusive neutrino nucleus processes and muon capture within a correlated local Fermi gas model (LFG), we discuss the relevance of nuclear finite-size effects in these reactions at low energy, in particular for muon capture. To disentangle these effects from others coming from the reaction dynamics we employ here a simple uncorrelated shell model that embodies the typical finite-size content of the problem. The integrated decay widths of muon atoms calculated with this shell model are then compared for several nuclei with those obtained within the uncorrelated LFG, using in both models exactly the same theoretical ingredients and parameters. We find that the two predictions are in quite good agreement, within 1–7%, when the shell model density and the correct energy balance is used as input in the LFG calculation. The present study indicates that, despite the low excitation energies involved in the reaction, integrated inclusive observables, like the total muon capture width, are quite independent of the fine details of the nuclear wave functions.

PACS. 23.40.Bw Weak-interaction and lepton (including neutrino) aspects – 25.30.-c Lepton-induced reactions – 21.60.Cs Shell model

1 Introduction

In this paper we study the importance of nuclear finite-size effects in inclusive muon capture reactions. The motivation for this investigation comes from the results of a recent publication [1,2], where we have developed a model which describes rather well the inclusive $^{12}\mathrm{C}(\nu_\mu, \mu^-)$ and $^{12}\mathrm{C}(\nu_e, e^-)$ cross-sections near threshold, and inclusive muon capture by nuclei. This approach, which is an extension of the quasi-elastic inclusive electron scattering model of [3], is based on a local Fermi gas (LFG), where the simplicity of the model makes it possible to include a great variety of effects into the reaction dynamics [4–8]. In particular, long-range nuclear correlations are taken into account by computing the RPA polarization propagator containing nucleonic and $\Delta(1232)$ degrees of freedom. All these effects are crucial for the correct analysis of atmospheric-neutrino fluxes [9–11] and to describe the recent neutrino experiments [12–17].

The results of [1], particularly those of muon capture, indicate that for some kind of inclusive reactions the validity of the LFG can be extended to energies lower than expected. Although the LFG leads to reasonable predictions for integrated quantities, at low energies it is not possible to describe the shape of the differential neutrino cross-section or muon capture width within this model. In fact both the discrete and the continuum states of the final nucleus, including giant resonances, contribute. However, when one sums over all the final states, the information about the fine details of the spectrum is lost and only the global contribution remains. Therefore, for some integrated inclusive observables, the results depend mainly on global quantities such as the correct energy balance or the nucleon distribution. An example is the inclusive pion capture model of [18,19]. The pioneering work of ref. [20] is also worthy of mention in the context of comparing shell model with Fermi gas for u-inclusive neutrino scattering.

The goal of this paper is to investigate whether finite-nucleus effects can affect significantly the LFG results of ref. [1] for inclusive muon capture. From the present calculation it is possible to estimate an uncertainty of 1–7% due to finite-size effects not taken into account in the LFG calculation of [1]. There already exist microscopic calculations of neutrino-nucleus reactions and muon capture, based on the RPA or large shell model (SM) basis [21–27], and other approaches such as the relativistic shell model [28] and the Green's function method [29]. All of them treat correctly the finite size of the system. However,

[a] e-mail: amaro@ugr.es

from direct comparison of these models with the LFG it is not possible to deduce the importance of the finite-nucleus treatment. The reason is that such comparison should be done between models embodying exactly the same nuclear dynamics. Instead, a great variety of residual interactions, shell model wave functions, current operators, Coulomb effects, etc., have been used in these works, making it impossible to disentangle the impact of the finite size on the different contributions.

Before such comparison be undertaken in a sophisticated framework, it is convenient to understand the uncorrelated case. For this reason we have chosen to perform this comparison with a simple model where the finite-size effects can be easily recognized. Thus, here we consider the extreme SM, *i.e.*, single-particle states in a Woods-Saxon (WS) potential, and we compare the results with those obtained from a LFG model. We do not include long-range correlations of RPA type or configuration mixing. In addition we use the static form of the single-nucleon charged current (CC), in order to simplify even more the calculation and to draw cleaner conclusions. On the other hand, within our simplified approach, we do not confine ourselves to the single case of ^{12}C, but make a more thorough study of how finite-size effects vary with increasing nuclear mass, by comparing the results for a set of closed-shell nuclei: ^{12}C, ^{16}O, ^{40}Ca, and ^{208}Pb.

The present calculation represents a first-stage test case to check the "equivalence" of LFG and shell models for some inclusive processes. We choose the μ-capture reaction for this investigation since it involves low excitation energies, the worst conditions for the LFG. Of course, under these simplifications it makes no sense to compare our results with the experimental data [30], nor it is the intention of this work, since it was already done in ref. [1] with the full model.

2 General formalism

2.1 Partial and differential width

Here we present the formalism to describe the inclusive muon capture within our model. We use Bjorken and Drell [31] conventions. We consider a negative muon bound into an initial nucleus ${}^{A}_{Z}X$, which decays into a final nucleus ${}^{A}_{Z-1}Y$ plus a muon neutrino (not detected),

$$\mu^- + {}^{A}_{Z}X \longrightarrow {}^{A}_{Z-1}Y + \nu_\mu \,. \tag{1}$$

The final nucleus can be in the discrete or in the continuum. We assume that the initial muon is in an s-wave state (normalized to one),

$$\phi_{1s}(\mathbf{r}) = \phi_{1s}(r) = \frac{R_{1s}(r)}{\sqrt{4\pi}}. \tag{2}$$

We describe the wave function ϕ_{1s} in a non-relativistic framework by solving the Schrödinger equation for the muon in the nuclear Coulomb potential, including finite-size and vacuum polarization effects. The final neutrino has four-momentum $k'^{\mu} = (\epsilon', \mathbf{k}')$. The leptonic current matrix element involved in the decay is then

$$\langle \nu_\mu | j^\mu(x) | \mu \rangle = \ell^\mu \phi_{1s}(x) e^{ik'\cdot x} \,, \tag{3}$$

where $x^\mu = (t, \mathbf{r})$ is the space-time coordinate, $\phi_{1s}(x)$ is the time-dependent muon wave function

$$\phi_{1s}(x) = \phi_{1s}(r) e^{-i\epsilon t} \tag{4}$$

and ϵ is its initial energy (including the binding). Since we treat the muon as non-relativistic, we describe its spin by a Pauli spinor χ which is contained into the leptonic vector ℓ^μ, defined by

$$\ell^\mu = \left[\frac{m'}{V\epsilon'}\right]^{1/2} \overline{u}_\nu(\mathbf{k}') \gamma^\mu (1-\gamma_5) u_\mu(0) \,, \tag{5}$$

where we have written the muon four-spinor as $u_\mu(0) = (\chi, 0)$, *i.e.*, corresponding effectively to a four-spinor with momentum zero. This is equivalent to neglecting in the following the initial muon momentum $\mathbf{k} = 0$ in the kinematics —however, the full spatial dependence of the wave function $\phi_{1s}(\mathbf{r})$ is maintained in the matrix element, see below. Finally in (5) V is the normalization volume of the neutrino plane wave, and m' its mass, that is set to zero at the end of the calculation.

The S-matrix element relevant for the decay reaction (1) is then

$$S_{fi} = -2\pi i \delta(E_f - E_i - \omega) \frac{G}{\sqrt{2}} \ell^\mu \langle f | \tilde{J}_\mu(-\mathbf{k}') | i \rangle \,, \tag{6}$$

where $|i\rangle$ and $|f\rangle$ are the initial and final nuclear states, with energies E_i and E_f, respectively, $\omega = \epsilon - \epsilon'$ is the energy transfer, $G = 1.1664 \times 10^{-5}\,\mathrm{GeV}^{-2} \cos\theta_c$ is the Fermi coupling constant multiplied by the cosine of Cabibbo's angle, and we have introduced the effective current operator $\tilde{J}_\mu$, defined in coordinate space as

$$\tilde{J}_\mu(\mathbf{r}) = J_\mu(\mathbf{r}) \phi_{1s}(r). \tag{7}$$

Here $J_\mu(\mathbf{r})$ is the nuclear CC operator to be specified below. Finally, $\tilde{J}_\mu(\mathbf{q})$ is the Fourier transform

$$\tilde{J}_\mu(\mathbf{q}) = \int \mathrm{d}^3 r e^{i\mathbf{q}\cdot\mathbf{r}} \tilde{J}_\mu(\mathbf{r}). \tag{8}$$

The differential decay width can be computed easily. Since the initial nucleus is unpolarized, the distribution of neutrinos is independent of the angles, and the corresponding angular integral gives a factor 4π.

At this point we have to distinguish two cases, depending on the kind of final state $|f\rangle$ reached. In the first case, the final nucleus is in a discrete state, that can be the ground state or an excited state. The neutrino energy takes discrete values fixed by energy conservation, and the partial width for the transition $i \to f$ is written as

$$\Gamma_{i\to f} = \frac{G^2}{2\pi} \frac{\epsilon'}{m} \eta^{\mu\nu} W^{i\to f}_{\mu\nu}(q) \,, \tag{9}$$

where $q = |\mathbf{q}|$, and the usual leptonic tensor has been introduced

$$\eta^{\mu\nu} = k^\mu k'^\nu + k^\nu k'^\mu - m\epsilon' g^{\mu\nu} + i\epsilon^{\mu\nu\alpha\beta} k_\alpha k'_\beta \qquad (10)$$

for initial muon momentum $k^\mu = (m, 0)$, where m is the muon mass. We have also defined the muon-hadronic tensor for the transition

$$W^{i\to f}_{\mu\nu}(q) = \overline{\sum_{M_f M_i}} \langle f|\tilde{J}_\mu(\mathbf{q})|i\rangle^* \langle f|\tilde{J}_\nu(\mathbf{q})|i\rangle \,, \qquad (11)$$

where $\mathbf{q} = \mathbf{k} - \mathbf{k}' = -\mathbf{k}'$ is the momentum transfer, we sum over final spin components M_f, and average over initial spins M_i.

In the second case, the final nucleus goes to the continuum, above the one-particle emission threshold, and the final neutrino energy ranges between 0 and the maximum energy available minus the nucleon separation energy of the final nucleus. The continuum spectrum of neutrinos is described by the differential decay width

$$\frac{\mathrm{d}\Gamma_c}{\mathrm{d}\epsilon'} = \frac{G^2}{2\pi}\frac{\epsilon'}{m}\eta^{\mu\nu} W^{(c)}_{\mu\nu}(q,\omega) \,, \qquad (12)$$

where now the continuum hadronic tensor is defined as

$$W^{(c)}_{\mu\nu}(q,\omega) = \overline{\sum_{fi}} \delta(E_f - E_i - \omega) \langle f|\tilde{J}_\mu(\mathbf{q})|i\rangle^* \langle f|\tilde{J}_\nu(\mathbf{q})|i\rangle \,. \qquad (13)$$

Here a sum over final (continuum) states and an average over initial spin is assumed.

The contraction between the leptonic and muon-hadronic tensor is easily performed in a coordinate system where the z-axis is in the $\mathbf{q}$ direction. We finally obtain the following expression for the differential decay width:

$$\frac{\mathrm{d}\Gamma_c}{\mathrm{d}\epsilon'} = \frac{G^2}{2\pi}\epsilon'^2 \left(R_C + R_L - 2R_{CL} + R_T + 2R_{T'}\right) \qquad (14)$$

and a similar expression for the discrete partial widths, where for simplicity the response functions have been introduced as the following components of the hadronic tensor [32,33]:

$$R_C = W^{00} \,, \qquad (15)$$

$$R_{CL} = -\frac{1}{2}\left(W^{03} + W^{30}\right) \,, \qquad (16)$$

$$R_L = W^{33} \,, \qquad (17)$$

$$R_T = W^{11} + W^{22} \,, \qquad (18)$$

$$R_{T'} = -\frac{i}{2}\left(W^{12} - W^{21}\right) \,. \qquad (19)$$

The total (inclusive) width is obtained by integrating and summing over the continuum and discrete, respectively,

$$\Gamma = \sum_f \Gamma_{i\to f} + \int_0^{\epsilon'_{\max}} \frac{\mathrm{d}\Gamma_c}{\mathrm{d}\epsilon'}\mathrm{d}\epsilon' \,. \qquad (20)$$

2.2 Multipole expansion

Since the shell model states have good angular momentum, $|i\rangle = |J_i M_i\rangle$, $|f\rangle = |J_f M_f\rangle$, it is usual to perform analytically the sums over third components using the Wigner-Eckart theorem. To this end one begins with the following multipole expansion valid for the components of any current operator in momentum space as a sum of operators with good angular momentum of rank J (note that the z-axis is in the $\mathbf{q}$ direction):

$$\tilde{J}_0(q) = \sqrt{4\pi}\sum_{J=0}^{\infty} i^J [J] \hat{C}_{J0}(q) \,, \qquad (21)$$

$$\tilde{J}_z(q) = -\sqrt{4\pi}\sum_{J=0}^{\infty} i^J [J] \hat{L}_{J0}(q) \,, \qquad (22)$$

$$\tilde{J}_m(q) = -\sqrt{2\pi}\sum_{J=0}^{\infty} i^J [J] \left[\hat{E}_{Jm} + m\hat{M}_{Jm}(q)\right], m = \pm 1 \,, \qquad (23)$$

where we use the notation $[J] \equiv \sqrt{2J+1}$, and in the last equation the spherical components of the current vector have been introduced $J_{\pm 1} = \mp(J_x \pm J_y)/\sqrt{2}$. The operators in this expansion are the usual Coulomb, longitudinal, transverse electric and transverse magnetic operators, defined by

$$\hat{C}_{J0}(q) = \int \mathrm{d}^3 r j_J(qr) Y_{J0}(\hat{\mathbf{r}}) \tilde{J}_0(\mathbf{r}) \,, \qquad (24)$$

$$\hat{L}_{J0}(q) = \frac{i}{q}\int \mathrm{d}^3 r \nabla \left[j_J(qr) Y_{J0}(\hat{\mathbf{r}})\right] \cdot \tilde{\mathbf{J}}(\mathbf{r}) \,, \qquad (25)$$

$$\hat{E}_{Jm}(q) = \frac{1}{q}\int \mathrm{d}^3 r \nabla \times \left[j_J(qr) \mathbf{Y}_{JJm}(\hat{\mathbf{r}})\right] \cdot \tilde{\mathbf{J}}(\mathbf{r}) \,, \qquad (26)$$

$$\hat{M}_{Jm}(q) = \int \mathrm{d}^3 r j_J(qr) \mathbf{Y}_{JJm}(\hat{\mathbf{r}}) \cdot \tilde{\mathbf{J}}(\mathbf{r}) \,, \qquad (27)$$

where j_J is a spherical Bessel function and $\mathbf{Y}_{JJm}$ is a vector spherical harmonic. Note that the above expansions (21)-(23) are a direct consequence of the familiar plane-wave expansion in spherical Bessel functions and spherical harmonics, inside the Fourier transform (8).

Inserting the expansions (21)-(23) inside the hadronic tensor (11), (13) we obtain

$$R_C = \frac{4\pi}{2J_i+1}\sum_J |C_J|^2 \,, \qquad (28)$$

$$R_L = \frac{4\pi}{2J_i+1}\sum_J |L_J|^2 \,, \qquad (29)$$

$$R_{CL} = \frac{2\pi}{2J_i+1}\sum_J \left(C_J^* L_J + L_J^* C_J\right) \,, \qquad (30)$$

$$R_T = \frac{4\pi}{2J_i+1}\sum_J \left(|E_J|^2 + |M_J|^2\right) \,, \qquad (31)$$

$$R_{T'} = -\frac{2\pi}{2J_i+1}\sum_J \left(E_J^* M_J + M_J^* E_J\right) \,, \qquad (32)$$

for the responses in the discrete, and a similar expression for the continuum responses with the addition of a sum over final states and a delta of energies $\sum_f \delta(E_f - E_i - \omega)$. The multipole coefficients in these sums are the reduced matrix elements of the corresponding multipole operators

$$C_J(q) = \langle f \| \hat{C}_J(q) \| i \rangle \,, \tag{33}$$

$$L_J(q) = \langle f \| \hat{L}_J(q) \| i \rangle \,, \tag{34}$$

$$E_J(q) = \langle f \| \hat{E}_J(q) \| i \rangle \,, \tag{35}$$

$$M_J(q) = \langle f \| \hat{M}_J(q) \| i \rangle \,. \tag{36}$$

The values of J and J_f are related by angular-momentum conservation $|J_i - J_f| \leq J \leq J_i + J_f$. In the particular case of closed-shell nuclei, such as ^{12}C, with $J_i = 0$, we have $J_f = J$.

2.3 Weak charged current

In order to simplify the comparison with the LFG, in this first stage we apply the above formalism to the CC $J^\mu = V^\mu - A^\mu$ in the static limit. This is not unreasonable for the μ-capture reaction since all the momenta involved are small. Thus, we only maintain the leading order in the standard expansion of the matrix element of the vector current

$$V^\mu(\mathbf{p}', \mathbf{p}) = \overline{u}(\mathbf{p}') \left[2F_1^V \gamma^\mu + i \frac{2F_2^V}{2M} \sigma^{\mu\nu} Q_\nu \right] u(\mathbf{p}) \tag{37}$$

in powers of p/M, p'/M, with M the nucleon mass, and $Q^\mu = (\omega, \mathbf{q})$ the four-momentum transfer ($Q^2 = \omega^2 - q^2$). Therefore, we take

$$V^0 \simeq 2F_1^V \,, \tag{38}$$

$$\mathbf{V} \simeq 0. \tag{39}$$

In the case of the axial current

$$A^\mu(\mathbf{p}', \mathbf{p}) = \overline{u}(\mathbf{p}') \left[G_A \gamma^\mu \gamma^5 + G_P Q^\mu \gamma^5 \right] u(\mathbf{p}) \tag{40}$$

we expand taking into account that, from PCAC, the pseudo-scalar form factor G_P is of order $O(M)$:

$$G_P = \frac{2M}{m_\pi^2 - Q^2} G_A \,, \tag{41}$$

and the leading-order term in the expansion of the axial current becomes

$$A^0 \simeq - \frac{G_A}{m_\pi^2 - Q^2} (\mathbf{q} \cdot \boldsymbol{\sigma}) \omega \,, \tag{42}$$

$$\mathbf{A} \simeq G_A \boldsymbol{\sigma} - \frac{G_A}{m_\pi^2 - Q^2} (\mathbf{q} \cdot \boldsymbol{\sigma}) \mathbf{q}. \tag{43}$$

Therefore, the total weak CC in the static limit that we use in the present work is

$$J^0 = J_V^0 - J_P^0 \,, \tag{44}$$

$$\mathbf{J} = - \mathbf{J}_A - \mathbf{J}_P \tag{45}$$

and the different terms in these equations are defined below. First-order terms in an expansion in powers of $1/M$ not included in our calculation can give an appreciable contribution, but the present approximation is enough for our purposes of testing the equivalence between LFG and shell models.

2.4 Multipole matrix elements of the current

The different multipoles of the vector, axial and pseudo-scalar currents (J_V^0, $\mathbf{J}_A$ and J_P^μ), introduced in eqs. (44), (45), are computed following the approach of ref. [34], where the matrix elements of the electro-weak neutral current were considered in the context of parity-violating electron scattering. In the case of the vector current we only consider the zero-th component to leading order $J_V^0 = 2F_1^V$. Therefore, only the Coulomb multipoles of this current enter our calculation. The reduced matrix elements between single-nucleon wave functions, with angular-momentum quantum numbers (l_p, j_p) and (l_h, j_h), are given by

$$\langle p \| \hat{C}_J(q) \| h \rangle = 2F_1^V P^+_{l_p + l_h + J} [J] \, a_J I_J(q). \tag{46}$$

Here we use the notation P_n^+ for the parity function (= 1 if n is even and 0 if n is odd), and we have defined the function $I_J(q)$ as

$$I_J(q) = \int_0^\infty \mathrm{d}r \, r^2 j_J(qr) R_p^*(r) R_h(r) \phi_\mu(r) \tag{47}$$

which contains the dynamical information on the nuclear transition and the muon wave function. Finally, the coupling coefficient a_J is defined in terms of a three-j coefficient:

$$a_J \equiv \frac{(-1)^{j_p + 1/2} [j_p][j_h]}{\sqrt{4\pi}} \begin{pmatrix} j_p & j_h & J \\ \frac{1}{2} & -\frac{1}{2} & 0 \end{pmatrix}. \tag{48}$$

In the case of the axial current we only consider the space components $\mathbf{J}_A = G_A \boldsymbol{\sigma}$ (we neglect the time component to leading order) so only the longitudinal and transverse (electric and magnetic) matrix elements enter:

$$\begin{aligned} \langle p \| \hat{L}_J^A(q) \| h \rangle = {} & i G_A P^+_{l_p + l_h + J + 1} \frac{a_J}{[J]} \\ & \times \left[(\kappa_p + \kappa_h - J) I_{J-1}(q) \right. \\ & \left. + (\kappa_p + \kappa_h + J + 1) I_{J+1}(q) \right] , \end{aligned} \tag{49}$$

$$\begin{aligned} \langle p \| \hat{E}_J^A(q) \| h \rangle = {} & - i G_A P^+_{l_p + l_h + J + 1} \frac{a_J}{\sqrt{J(J+1)}[J]} \\ & \times \left[(J + 1 + \kappa_p + \kappa_h) J I_{J+1}(q) \right. \\ & \left. + (J - \kappa_p - \kappa_h)(J+1) I_{J-1}(q) \right] , \end{aligned} \tag{50}$$

$$\begin{aligned} \langle p \| \hat{M}_J^A(q) \| h \rangle = {} & G_A P^+_{l_p + l_h + J} \frac{a_J [J]}{\sqrt{J(J+1)}} \\ & \times (\kappa_p - \kappa_h) I_J(q) \,, \end{aligned} \tag{51}$$

where we use the notation $\kappa_p = (-1)^{j_p + l_p + \frac{1}{2}} (j_p + \frac{1}{2})$. Note that the longitudinal and electric multipoles have abnormal parity, *i.e.*, $l_p + l_h + J =$ odd as expected for an axial current.

In the case of the pseudo-scalar current $J^\mu_P = -\frac{G_A}{m_\pi^2-Q^2}(\mathbf{q}\cdot\boldsymbol{\sigma})Q^\mu$, the multipoles can be related to the longitudinal components of the axial current $J^z_A = G_A\boldsymbol{\sigma}\cdot\hat{\mathbf{q}}$. Using expansion (22) for the longitudinal current we have for the zero-th component

$$J^0_P = -\frac{\omega q}{m_\pi^2-Q^2}J^z_A \tag{52}$$

$$= \frac{\omega q}{m_\pi^2-Q^2}\sqrt{4\pi}\sum_J i^J[J]\hat{L}^A_{J0}. \tag{53}$$

Comparing with expansion (21) we obtain that the Coulomb operators of the pseudo-scalar current are proportional to the longitudinal multipoles of the axial current,

$$\hat{C}^P_{J0} = \frac{\omega q}{m_\pi^2-Q^2}\hat{L}^A_{J0} \tag{54}$$

and the same relation holds for the matrix elements. Since the spatial part of the pseudo-scalar current is proportional to $\mathbf{q}$, it has no transverse components. Only the longitudinal multipoles enter, that are again proportional to the axial ones

$$\hat{L}^P_{J0} = -\frac{q^2}{m_\pi^2-Q^2}\hat{L}^A_{J0}. \tag{55}$$

and a similar relation between the corresponding matrix elements.

Finally, note that in the present static approximation, where there are no transverse multipoles for the vector current, the response function $R_{T'} = 0$, because only the interference between electric and magnetic multipoles of the vector and axial current, respectively (and vice versa) would enter eq. (32).

2.5 The local Fermi gas

In the local Fermi gas model we first compute the decay width $\Gamma_{FG}[\rho_P,\rho_N]$ for a muon at rest inside a Fermi gas with constant proton and neutron densities

$$\rho_P = k^3_{FP}/3\pi^2, \qquad \rho_N = k^3_{FN}/3\pi^2, \tag{56}$$

where k_{FP} and k_{FN} are the Fermi momenta of protons and neutrons, respectively. With the charged current (44), (45), the response functions (15)-(19) are computed in this model using the formalism of [1,34]. The final result can be written simply as

$$\frac{\mathrm{d}\Gamma_{FG}}{\mathrm{d}\epsilon'} = \frac{G^2}{\pi}\epsilon'^2\left[4F^2_{1V} + G^2_A(3+C^2_P-2C_P)\right]R_0\,, \tag{57}$$

where we have defined the following factor coming from the pseudo-scalar current:

$$C_P \equiv \frac{m\epsilon'}{m_\pi^2-Q^2}, \tag{58}$$

and the function R_0 is related to the imaginary part of the Linhard function [1,34]

$$2R_0 = -\frac{1}{\pi}\mathrm{Im}\,\overline{U} = \frac{M^2}{2\pi^2 q}\theta(\epsilon_{FP}-\epsilon_0)(\epsilon_{FP}-\epsilon_0). \tag{59}$$

Here we have defined

$$\epsilon_0 = \mathrm{Max}\left\{\epsilon_{FN}-\omega, \frac{1}{2M}\left(\frac{M\omega}{q}-\frac{q}{2}\right)^2\right\} \tag{60}$$

and $\epsilon_{FP} = k^2_{FP}/2M$ is the Fermi energy of protons, and $\epsilon_{FN} = k^2_{FN}/2M$ for neutrons. The LFG width is then obtained by inserting the proton and neutron densities, $\rho_P(\mathbf{r})$ and $\rho_N(\mathbf{r})$, of the finite-size nucleus into eq. (56) and averaging with the muon density [1]

$$\Gamma_{LFG} = \int \mathrm{d}^3r|\phi_\mu(\mathbf{r})|^2\Gamma_{FG}[\rho_P(\mathbf{r}),\rho_N(\mathbf{r})]. \tag{61}$$

An important input for the LFG is the experimental Q-value for the reaction (1)

$$Q = M(^A_{Z-1}Y) - M(^A_ZX) = \omega_{\min} \tag{62}$$

which is the minimum value allowed for the energy transfer ω. In order to account for this value in the Fermi gas, we substitute ω by $\omega - Q$, since part of the energy ω is employed in producing the final nucleus. In this way we treat correctly the energy balance, which is important for describing the experimental muon capture width [1]. When different densities are used for protons and neutrons, especially in the case of ^{208}Pb, there is a gap,

$$\epsilon_{\mathrm{gap}} = \epsilon_{FN} - \epsilon_{FP}\,, \tag{63}$$

between neutron and proton Fermi energies, that has to be considered also in the energy balance by substituting

$$\omega \longrightarrow \omega + \epsilon_{\mathrm{gap}} - Q. \tag{64}$$

3 Results

In this section we present results for a set of closed-shell nuclei ^{12}C, ^{16}O, ^{40}Ca, and ^{208}Pb. In the extreme shell model the initial and final nuclear wave function are described as Slater determinants constructed with single-particle wave functions that are solutions of the Schrödinger equation with a Woods-Saxon potential

$$V(r) = V_0 f(r,R_0,a_0) - V_{LS}\frac{2\boldsymbol{l}\cdot\boldsymbol{\sigma}}{r}\frac{\mathrm{d}f(r,R_0,a_0)}{\mathrm{d}r} + V_C(r), \tag{65}$$

where

$$f(r,R_0,a_0) = \frac{1}{1+e^{(r-R_0)/a_0}} \tag{66}$$

and $V_C(r)$ is, for protons, the Coulomb potential of a charged sphere of charge $Z-1$ and radius R_C, and it is equal to zero for neutrons. The parameters of the potential are commonly fitted to the experimental energies of the valence shells or the charge radius. In the present case of muon capture we fit the experimental Q-value (62) for the decay reaction (1). In the shell model, the energy difference between hadronic final and initial states is computed as the difference between the corresponding shells

$$\omega = \epsilon_p - \epsilon_h\,, \tag{67}$$

Table 1. Parameters of the Woods-Saxon potentials used in ^{12}C, ^{16}O and ^{40}Ca for protons (P) and neutrons (N). The units are MeV for V_i, and fm for a_0 and r_0. The reduced radius parameter r_0 is defined by $R_0 = r_0 A^{1/3}$. The Coulomb radius is chosen as $R_C = R_0$.

		V_0^P	V_{LS}^P	V_0^N	V_{LS}^N	r_0	a_0
^{12}C	WS1	−52.38	−20.30	−50.85	−24.11	1.25	0.57
	WS2	−62.38	−3.20	−50.85	−18.40		
	WS3	−62.38	−3.20	−38.30	−3.15		
^{16}O	WS1	−52.50	−0.60	−52.50	−0.60	1.27	0.53
	WS2	−52.50	−7.00	−42.80	−6.54		
	WS3	−50.00	0.00	−50.00	0.00		
^{40}Ca	WS1	−50.45	−4.83	−48.66	−5.20	1.25	0.53
	WS2	−57.50	−11.11	−55.00	−2.30		
	WS3	−57.50	−11.11	−53.00	−5.10		

Table 2. Parameters of the Woods-Saxon potentials of ^{208}Pb for protons (P) and neutrons (N). Note that we use different radius parameters for the central and spin-orbit parts of the potential. The units are MeV for V_i, and fm for a_i and r_i. The reduced radius parameters r_i are defined by $R_i = r_i A^{1/3}$. The Coulomb radius is chosen as $R_C = R_0$.

		V_0	V_{LS}	r_0	a_0	r_{LS}	a_{LS}
WS1	P	−60.4	−7.45	1.26	0.79	1.21	0.59
	N	−46.9	−5.64	1.21	0.66	1.17	0.64
WS2	P	−60.4	−6.75	1.26	0.79	1.22	0.59
	N	−43.5	−6.08	1.26	0.66	1.17	0.64

where ϵ_p and ϵ_h are eigenvalues of the Schrödinger equation for particles (neutrons) and holes (protons), respectively. Therefore, the Q-value (62) is obtained in this model as the energy difference between the first unoccupied neutron shell and the last occupied proton shell, corresponding to the transition of a valence proton to a neutron above the Fermi level. This makes only one condition for fixing the several parameters of the potential (65). Wherever possible, we set the remaining parameters of the potential to values similar to the ones used in other studies like those of refs. [18,34,35]. In our calculation we use different sets of parameters, denoted WS1, WS2 and WS3, shown in table 1 for ^{12}C, ^{16}O, ^{40}Ca, and in table 2 for ^{208}Pb.

The only states relevant for μ-capture are the occupied proton holes and the neutron particles above the valence shell. In the discrete sector several transitions are possible with fixed excitation energies. The single-particle energies of the last occupied proton shell and first unoccupied neutron shell obtained with the potentials of tables 1, 2 are shown in table 3. The Q-value corresponds to the transition $P \longrightarrow N$ in table 3, with an energy difference

$$Q = \epsilon(N) - \epsilon(P) \tag{68}$$

which is also shown in table 3, together with the experimental value $Q_{\rm exp}$ in the last column. The number of discrete neutron states is finite. Above the last discrete neutron state, the next allowed transitions are to the continuum. The continuum neutron states are obtained by solving the Schrödinger equation for positive energies. More details on the continuum solutions can be found in refs. [18,34,35].

Table 3. Single-particle energies in MeV used in the fit of the Q-value for μ-capture (the experimental values are shown in the last column).

Nucleus		WS1	WS2	WS3	Exp.
^{12}C	$P1p_{3/2}$	−15.96	−18.38	−18.13	
	$N1p_{1/2}$	−2.08	−4.50	−4.25	
	Q-value	13.88	13.88	13.88	13.880
^{16}O	$P1p_{1/2}$	−15.31	−12.77	−13.76	
	$N1d_{5/2}$	−4.39	−1.84	−2.83	
	Q-value	10.92	10.93	10.93	10.931
^{40}Ca	$P1d_{3/2}$	−8.33	−8.78	−8.78	
	$N1f_{7/2}$	−6.51	−6.95	−6.95	
	Q-value	1.83	1.83	1.83	1.822
^{208}Pb	$P3s_{1/2}$	−8.19	−8.19		
	$N2g_{9/2}$	−2.68	−2.68		
	Q-value	5.51	5.51		5.512

Table 4. Integrated width in units of $10^5\,{\rm s}^{-1}$ for the different nuclei and Woods-Saxon potentials, compared with the LFG results using the corresponding charge densities. The discrete contribution of the shell model is shown in the first column.

		Discrete	Total	LFG	%
^{12}C	WS1	0.3115	0.4406	0.4548	3.2
	WS2	0.3179	0.4289	0.4360	1.7
	WS3	0.2746	0.5510	0.4732	−14.1
^{16}O	WS1	1.113	1.282	1.360	6.1
	WS2	0.590	1.118	1.392	24.3
	WS3	1.154	1.332	1.387	4.1
^{40}Ca	WS1	29.10	37.12	36.73	−1.1
	WS2	27.79	33.79	34.90	3.3
	WS3	26.28	32.73	35.03	7.0
^{208}Pb	WS1	215.6	390.3	399.4	2.3
	WS2	266.8	467.4	439.5	−5.9

In order to compare with the LFG, it is important to use as input the proton and neutron densities obtained in the corresponding shell model, by summing over occupied states as follows:

$$\rho_P(\mathbf{r}) = \sum_{\rm protons} \frac{2j+1}{4\pi} |R_{nlj}(r)|^2, \tag{69}$$

where $R_{nlj}(r)$ are the radial wave functions, and a similar expression for neutrons.

The shell model calculation has been checked by comparison with the factorized plane-wave impulse approximation (PWIA) [36]. In this approximation there is no final-state interaction and hence the final neutron states are plane waves. The transition matrix elements appearing in the hadronic tensor (13) are computed trivially in terms of the product of a single-nucleon current matrix element times the Fourier transform of a nuclear overlap

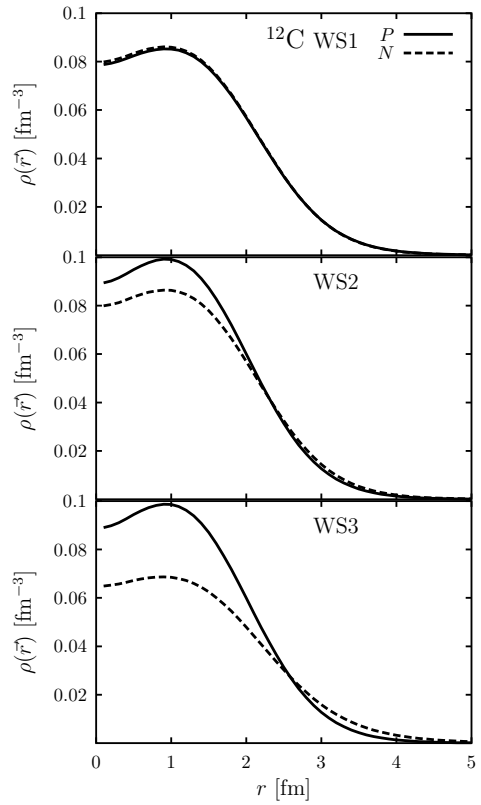

Fig. 1. Proton and neutron densities of ^{12}C for the several WS potentials used in this work.

function of the missing momentum, in a way which is similar to the analysis of exclusive $(e, e'p)$ reactions [37] (but this time the nuclear overlap function includes the bound-muon wave function). As a consequence, the exclusive hadronic tensor factorizes as the product of a single-nucleon hadronic tensor times a partial-momentum distribution, and the calculation is straightforward in the shell model. For the present case an additional integration and a sum over initial states is needed since we are interested in the inclusive case, similar to the factorized PWIA in (e, e') introduced in [36]. The PWIA can be also approached with our multipole-expansion code by setting to zero the WS potential in the final states. This allows us to check the multipole-expansion calculation and, at the same time, to fix the number of multipoles in the sum over J, eqs. (21)-(23). The differences with the factorized calculations are negligible when we include up to five multipoles.

In table 4 we show results for the integrated inclusive widths for the four nuclei and for the different models used in this work. For each one of the WS parameterizations we show in the second column the contribution to the width from the discrete final neutron states, while in the third column we show the total width (discrete + continuum). The LFG results are shown in the fourth column, and for comparison we show the percentual relative difference between LFG and WS in the last column. Next we discuss the results obtained for each one of the nuclei studied in this work.

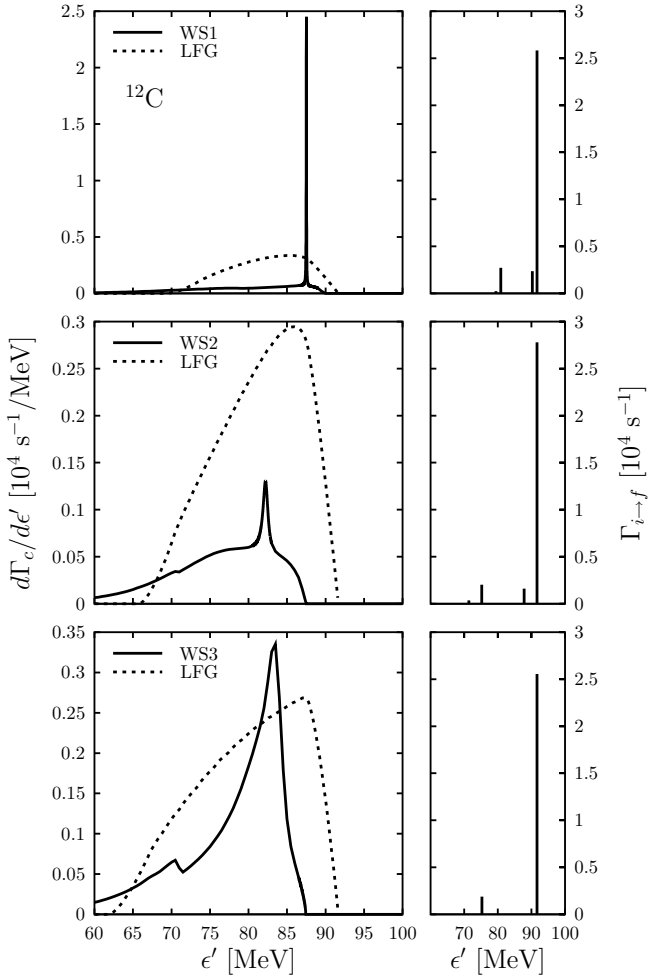

Fig. 2. Differential SM width of ^{12}C to the continuum (left panels) compared to the LFG, and partial widths to the discrete states (right panels), as a function of the neutrino energy, for the different WS potentials considered in this work.

3.1 ^{12}C

In table 4 we can see that, in the case of WS1 and WS2, the LFG and WS results for ^{12}C are quite similar, differing only in $\sim$ 2–3%. In the case of WS3 the differences are larger, around 14%.

All the WS potential parameters have been fitted to the experimental Q-value (68), which, in the SM, is the difference between the neutron $p_{1/2}$ and proton $p_{3/2}$ energies. Among all the potentials, WS1 is the more realistic since it also fits the proton and neutron separation energies of ^{12}C and give reasonable masses for the ground states of the ^{13}N and ^{13}C nuclei. When we use similar parameters for protons and neutrons, like in WS1, we need a large spin-orbit splitting in order to fit the experimental Q-value. In the case of the potential WS2 we use different parameters for protons and neutrons: The proton well is similar to the one of ref. [34], that is more attractive than WS1, with small spin-orbit strength. The neutron parameters are similar to WS1. Finally, in WS3 we have used a small neutron spin-orbit splitting, as for protons, but we

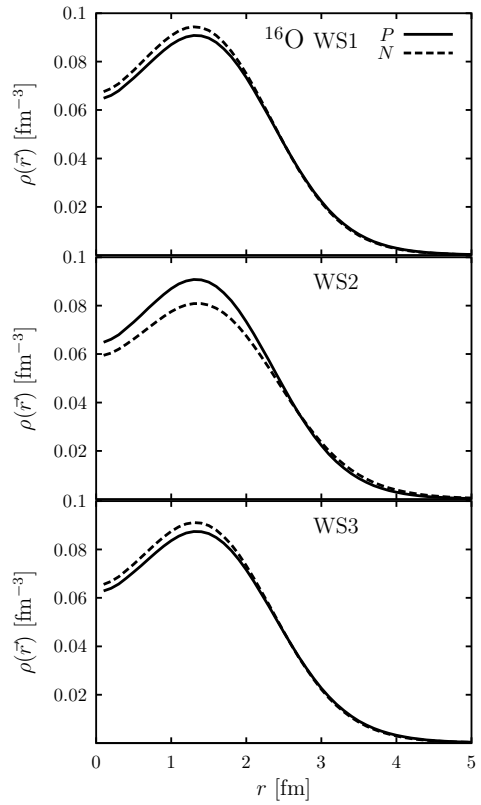

Fig. 3. The same as fig. 1 for ^{16}O.

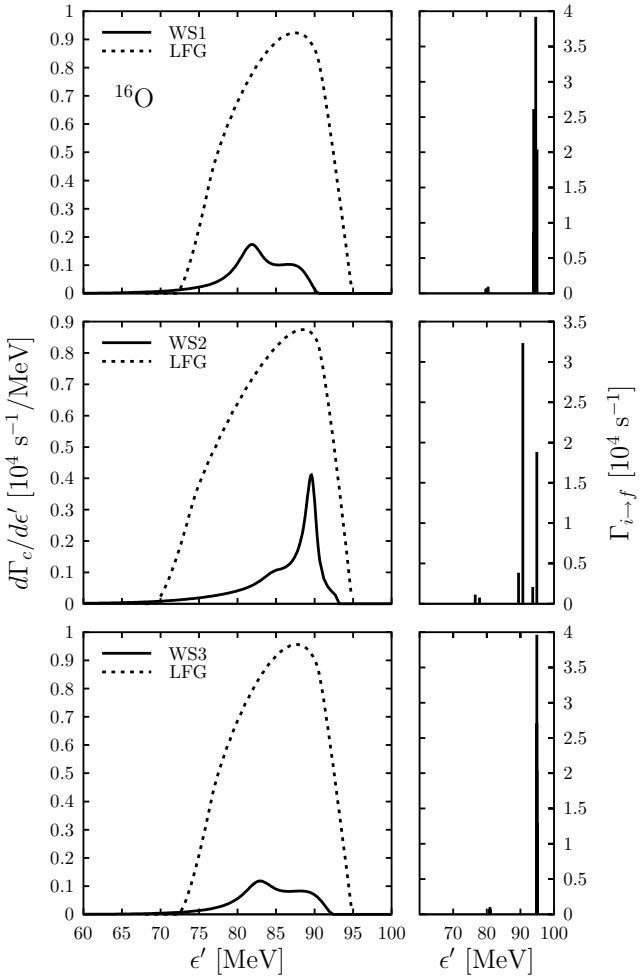

Fig. 4. The same as fig. 2 for ^{16}O.

had to make the neutron well much less attractive than for protons. Apart from changing the single-particle energies, the effect of modifying the WS potential can be appreciated in the proton and neutron densities shown in fig. 1. For more attractive potentials the nucleus becomes denser in the interior. For this reason, the WS3 neutron density turns out to be the smallest one, while the proton density is around 3/2 the neutron one. Hence, the LFG results are worse for very different neutron and proton densities. In this situation, the proton and neutron Fermi momenta (56) are clearly different, leading to a gap between proton and neutron energies, (63), which, in this case, is negative, since the density is smaller for neutrons, and $\epsilon_{FN} < \epsilon_{FP}$. Therefore, a proton near the Fermi surface can decay to a neutron above the neutron Fermi surface with an energy decrement. This is an unrealistic situation, since precisely in this case the neutrons are less bound than protons in the SM, and therefore lie at higher energies. Another argument to disregard this case is the well-known property of closed-(sub)shell nuclei such as ^{12}C, for which the neutron and proton densities should be similar. Note that in all cases the gap between the N and P Fermi species has been taken into account in the energy balance by the replacement (64).

In fig. 2 we compare the SM results for the differential width to the continuum with the LFG distribution for the different WS parameters (left panels). The shapes of both distributions are completely different. The differences are more apparent for the WS1 potential, where there is a very high and sharp neutron resonance in the SM spectrum. The partial widths to the discrete states are shown in the right panels of fig. 2. Considering these differences in shape between the LFG and the SM, it is a very notable result that the integrated widths (adding the discrete states) take similar values in both models as was shown in table 4. This outcome agrees with the findings of ref. [38], where the same problem was addressed in the context of inelastic electron scattering on nuclei.

The biggest contribution to the width comes in all the cases from the transition to the ground state, and its magnitude does not depend very much on the potential, since in the transition $p_{3/2} \to p_{1/2}$ the wave functions in the initial and final states are similar across the different potentials. Note also that there are transitions to final discrete states that lie in the continuum (particularly, transitions from the $1s$ shell). These states will contribute to the giant resonances after an appropriate treatment of the residual interaction (such as in the RPA). Under the light of the present preliminary study and the results of ref. [1] one expects that the inclusion of the RPA does not change too much our conclusions and the total integrated width be similar for correlated LFG and SM.

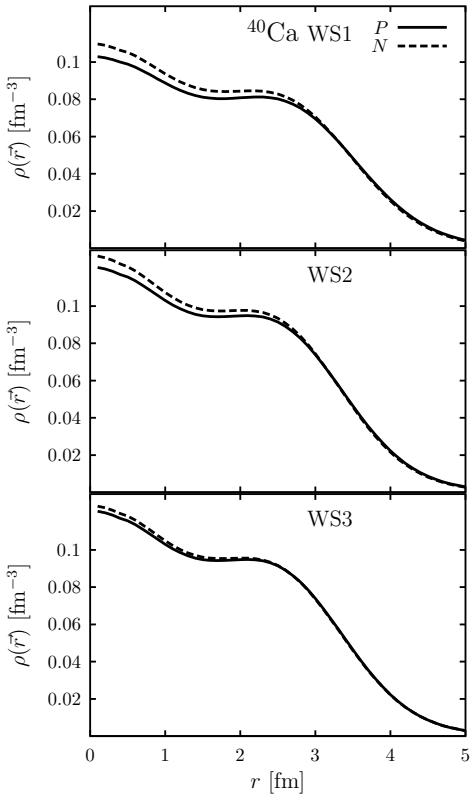

Fig. 5. The same as fig. 1 for ^{40}Ca.

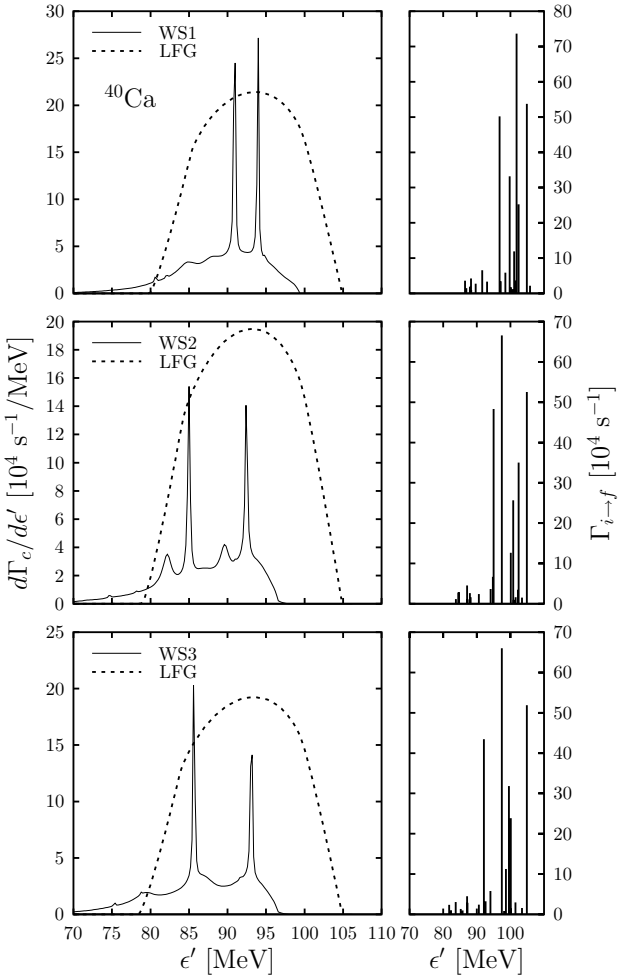

Fig. 6. The same as fig. 2 for ^{40}Ca.

3.2 ^{16}O

In the case of ^{16}O the integrated widths computed in the LFG are also very close, $\sim$ 4–6%, to the SM results with the potentials WS1 and WS3 (see table 4). The worst results are obtained for the WS2 parameterization; the corresponding width is 24% of the SM one. This can also be understood in terms of what was said for the case of ^{12}C above, by looking at the ^{16}O densities shown in fig. 3. The case of WS2 is the only one where the protons are more bound than the neutrons, hence the N-density is smaller than the P-density inside the nucleus, which is again an unrealistic situation because one expects the opposite in a closed-shell nucleus such as ^{16}O.

We should add that the ^{16}O nucleus is delicate in the sense that the experimental Q-value of 10.93 MeV is too large to be fitted by the WS parameters found in the literature [18,34]. In fact, in the SM the Q-value is the difference between the $N1d_{5/2}$ and $P1p_{1/2}$ energies (see table 3). The effect of the spin-orbit potential is to increase $\epsilon(p_{1/2})$ and to decrease $\epsilon(d_{5/2})$, that is, it goes to reduce the Q-value. (The opposite happens for ^{12}C, where the Q-value is the difference between the $Np_{1/2}$ and $Pp_{3/2}$ energies. Hence, the spin-orbit goes to increase the Q-value.) Therefore, to make that value as large as 11 MeV one needs a small spin-orbit potential, as in WS1, or to raise the neutron well with respect to the proton well, as in WS2, at the cost of making the neutrons less bound than protons. The first option is preferred because it allows for similar proton and neutron densities. Precisely the third parameterization WS3 has been chosen with $V_{LS} = 0$ to maximize the difference between these two shells.

The differential and partial widths of ^{16}O for the three WS potentials are shown in fig. 4. In the three cases the main contribution comes from the discrete spectrum (see also table 4). Since $V_{LS} = 0$ for WS3, the dominant contribution comes from transitions from the $1p$ to the $1d$ shell.

3.3 ^{40}Ca

The LFG results improve when the mass of the nucleus increases as in the present case of the nucleus ^{40}Ca. In fact, from table 4 we see that for this nucleus the LFG integrated width is within 1% of the SM result for WS1, and 3% and 7% in the other two cases. This improvement was expected because the Fermi gas description of the nucleus should work better for heavier nuclei. In the case of WS2 and WS3 the proton parameters have been fixed to the typical values used in the literature, and we have fitted the neutron ones. Since here the experimental Q-value is small, $Q = 1.8$ MeV, one does not need to change too

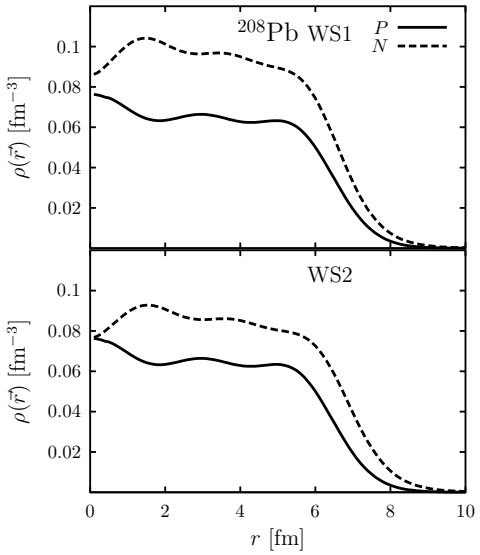

Fig. 7. The same as fig. 1 for ^{208}Pb.

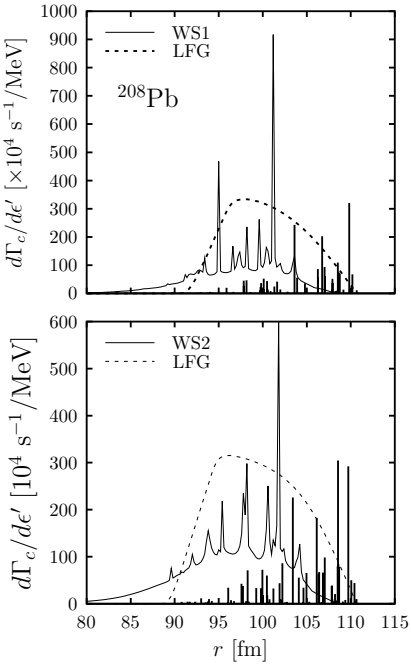

Fig. 8. The same as fig. 2 for ^{208}Pb. In this case we show the discrete contributions in units of $10^4\,\mathrm{s}^{-1}$ in the same panel as the continuum one.

much the typical neutron parameters. In the case of WS1 we have tried to maintain the P and N parameters similar. The proton and neutron densities are close in all cases, as shown in fig. 5, and the proton levels always lie above the neutron ones.

The neutrino spectrum shown in fig. 6 presents a more complex structure than the lighter nuclei discussed above. More potential resonances arise and the discrete spectrum presents more lines distributed along the allowed energy region.

3.4 ^{208}Pb

Finally we discuss the results for the closed-shell heavy nucleus ^{208}Pb. In table 4 we present integrated widths only for two sets of potential parameters, WS1 and WS2. This is the only case where we use different radius parameters for protons and neutrons and also for the central and spin-orbit parts of the potential, see table 2. In both cases the LFG results are close, within 3 and 6%, to the SM ones. The Q-value, 5.5 MeV, is close to the $N2g_{9/2}$ and $P3s_{1/2}$ energy difference of typical parameterizations [34,39]. Only small variations of these parameterizations found in the literature are allowed if one wants to maintain the ordering of the energies around the Fermi level. Also only small variations are needed to fit the experimental Q-value. In the present case the treatment of asymmetric nuclear matter is essential, because the proton and neutron densities, shown in fig. 7, are clearly different. Therefore, the correct treatment of the gap in the energy balance, eqs. (63), (64), is needed to obtain the results of table 4. Moreover, in this case the neutrino spectrum shown in fig. 8 shows also an improved resemblance between the LFG and SM (although numerous potential resonances appear), even taking into account the distribution of the discrete spectrum.

4 Conclusions

In this paper we have estimated the magnitude of the finite-nucleus effects on inclusive muon capture, aiming at quantifying the uncertainty of the LFG results of ref. [1]. It is not possible to disentangle these effects by comparison with the highly sophisticated RPA or shell models existing in the literature due to the different theoretical ingredients embodied in them.

To know how much the LFG is modified by finite-size effects, one would need a finite-nucleus model with exactly the same input as the LFG, in order to make the comparison meaningful. Obviously this would be a drawback precisely because one wants to use the LFG due to its simplicity, in order to include very complex dynamical effects hard to incorporate in finite-nucleus treatments. Therefore, before using a very sophisticated model, it is convenient to see what happens in the uncorrelated case.

In this paper we have focused on a simple shell model without nuclear correlations, but that contains the relevant information about the finite nuclear structure, and we have compared it with the uncorrelated LFG using the same input. In particular, the SM proton and neutron densities have been used in the LFG calculation. We have applied both models to a set of closed-shell nuclei: ^{12}C, ^{16}O, ^{40}Ca, and ^{208}Pb. In the SM we fit the experimental Q-value of the decay, while the same value is used to correct the energy transfer in the LFG, taking into account also the gap between neutron and proton Fermi energies. As expected, the neutrino spectrum is very different in both models, in particular the LFG cannot account for the resonances and discrete states. However, in the case

of the lighter nuclei, ^{12}C and ^{16}O, the SM and LFG results for the integrated width are close —within 3–6%— for WS parameters with similar neutron and proton densities, but the results are somewhat different, within 14–24%, for the disregarded cases in which the protons lie below the neutrons. For the medium and heavy nuclei, ^{40}Ca and ^{208}Pb, the integrated widths are always very close, within 1–7%. The final neutrino spectrum of the LFG becomes more similar to the SM, including the discrete part, for heavier nuclei. Under the assumption that RPA correlations and finite-size effects are somewhat decoupled for integrated inclusive observables, the present results can explain why the LFG results of ref. [1] describe so well the experimental data.

This work was partially supported by funds provided by DGI (Spain) and FEDER funds, under Contract No. BFM2002-03218, and by the Junta de Andalucía.

References

1. J. Nieves, J.E. Amaro, M. Valverde, Phys. Rev. C **70**, 055503 (2004).
2. J. Nieves, J.E. Amaro, M. Valverde, Nucl. Phys. B (Proc. Suppl.) **139**, 195 (2005).
3. A. Gil, J. Nieves, E. Oset, Nucl. Phys. A **627**, 543; 598 (1997).
4. H.C. Chiang, E. Oset, P. Fernández de Córdoba, Nucl. Phys. A **510**, 591 (1990).
5. N.C. Mukhopadhyay, H.C. Chiang, S.K. Singh, E. Oset, Phys. Lett. B **434**, 7 (1998).
6. S.K. Singh, E.Oset, Phys. Rev. C **48**, 1246 (1993).
7. T.S. Kosmas, E. Oset, Phys. Rev. C **53**, 1409 (1996).
8. S.K. Singh, N.C. Mukhopadhyay, E. Oset, Phys. Rev. C **57**, 2687 (1998).
9. See, for instance, talks at *The Third Workshop on Neutrino-Nucleus Interactions in the Few GeV Region (NuInt04), Gran Sasso, 2004*, `http://nuint04.lngs.infn.it`.
10. Y. Fukuda *et al.*, Phys. Rev. Lett. **81**, 1562 (1998).
11. K. Zuber, Phys. Rep. **305**, 6 (1998).
12. D.A. Krakauer *et al.*, Phys. Rev. C **45**, 2450 (1992).
13. B.E. Bodmann *et al.*, Phys. Lett. B **332**, 251 (1994).
14. L.B. Auerbach *et al.*, Phys. Rev. C **64**, 065501 (2001).
15. M. Albert *et al.*, Phys. Rev. C **51**, 1065 (1995).
16. C. Athanassopoulos *et al.*, Phys. Rev. C **56**, 2806 (1997).
17. L.B. Auerbach *et al.*, Phys. Rev. C **66**, 015501 (2002).
18. J.E. Amaro, A.M. Lallena, J. Nieves, Nucl. Phys. A **623**, 529 (1997);
19. H.C. Chiang *et al.*, Nucl. Phys. A **510**, 573 (1990); **514** 749 (1990)(E).
20. M.B. Barbaro, A. De Pace, T.W. Donnelly, A. Molinari, M.J. Musolf, Phys. Rev. C **54**, 1954 (1996).
21. D.F. Measday, Phys. Rep. **354**, 243 (2001).
22. E. Kolbe, K. Langanke, P. Vogel, Phys. Rev. C **50**, 2576 (1994).
23. E. Kolbe, K. Langanke, P. Vogel, Phys. Rev. C **62** 055502 (2000).
24. E. Kolbe, K. Langanke, P. Vogel, Nucl. Phys. A **652**, 91 (1999).
25. A.C. Hayes, I.S. Towner, Phys. Rev. C **61**, 044603 (2000).
26. C. Volpe, N. Auerbach, G. Colo, T. Suzuki, N. Van Giai, Phys. Rev. C **62**, 015501 (2000).
27. F. Krmpotić, A. Samana, A. Mariano, Phys. Rev. C **71**, 044139 (2005).
28. C. Maieron, M.C. Martinez, J.A. Caballero, J.M. Udias, Phys. Rev. C **68**, 048501 (2003).
29. A. Meucci, C. Giusti, F.D. Pacati, Nucl. Phys. A **739**, 277 (2004).
30. T. Suzuki, D.F. Measday, J.P. Roalsvig, Phys. Rev. C **35**, 2212 (1987).
31. J.D. Bjorken, S.D. Drell, *Relativistic Quantum Mechanics* (McGraw-Hill, 1965).
32. T.W. Donnelly, R.D. Peccei, Phys. Rep. **50**, 1 (1979).
33. J.E. Amaro, M.B. Barbaro, J.A. Caballero, T.W. Donnelly, A. Molinari, I. Sick, Phys. Rev. C **71**, 015501 (2005).
34. J.E. Amaro, J.A. Caballero, T.W. Donnelly, E. Moya de Guerra, A.M. Lallena, J.M. Udias, Nucl. Phys. A **602**, 263 (1996).
35. C. Albertus, J.E. Amaro, J. Nieves, Phys. Rev. C **67**, 034604 (2003).
36. J.E. Amaro, J.A. Caballero, T.W. Donnelly, E. Moya de Guerra, Nucl. Phys. A **611**, 163 (1996).
37. M. Mazziotta, J.E. Amaro, F. Arias de Saavedra, Phys. Rev. C **65**, 034602 (2002).
38. R. Cenni, T.W. Donnelly, A. Molinari, Phys. Rev. C **56**, 276 (1997).
39. J.S. Dehesa, PhD Thesis, Universität Bonn (1977), unpublished.